ACSNANO

www.acsnano.org

ARTICLE

Dye Quenching of Carbon Nanotube Fluorescence Reveals Structure-Selective Coating Coverage

Yu Zheng, Ali A. Alizadehmojarad, Sergei M. Bachilo, Anatoly B. Kolomeisky, and R. Bruce Weisman*

Cite This: *ACS Nano* 2020, 14, 12148−12158

Read Online

ACCESS | Metrics & More | Article Recommendations | Supporting Information

ABSTRACT: Many properties and applications of single-wall carbon nanotubes (SWCNTs) depend strongly on the coatings that allow their suspension in aqueous media. We report that SWCNT fluorescence is quenched by reversible physisorption of dye molecules such as methylene blue, and that measurements of that quenching can be used to infer structure-specific exposures of the nanotube surface to the surrounding solution. SWCNTs suspended in single-stranded DNA oligomers show quenching dependent on the combination of nanotube structure and ssDNA base sequence. Several sequences are found to give notably high or low surface coverages for specific SWCNT species. These effects seem correlated with the selective recognitions used for DNA-based structural sorting of nanotubes. One notable example is that dye quenching of fluorescence from SWCNTs coated with the $(ATT)_4$ base sequence is far stronger for one (7,5) enantiomer than for the other, showing that coating coverage is associated with the coating affinity difference reported previously for this system. Equilibrium modeling of quenching data has been used to extract parameters for comparative complexation constants and accessible surface areas. Further insights are obtained from molecular dynamics simulations, which give estimated contact areas between ssDNA and SWCNTs that correlate with experimentally inferred surface exposures and account for the enantiomeric discrimination of $(ATT)_4$.

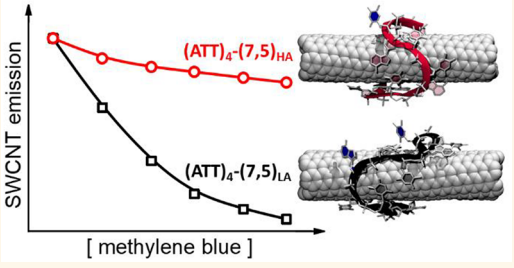

KEYWORDS: *single-stranded DNA, single-wall carbon nanotube, SWCNT enantiomer, methylene blue, physisorbed quencher, specific recognition, molecular dynamics*

Single-wall carbon nanotubes (SWCNTs) are a family of one-dimensional artificial nanomaterials with unusual physical and chemical properties and numerous potential applications. Bulk samples of as-grown SWCNTs contain many discrete structural species, each of which is labeled by a pair of integers (n,m).[1] Except for the achiral structures, $n = m$ or $m = 0$, each species also exists in two enantiomeric forms. Because of their inherent hydrophobicity, pristine SWCNTs can be individually dispersed in water only when their sidewall surfaces are noncovalently coated by surfactants or amphiphilic polymers.[2−7] These coatings play crucial roles in many SWCNT processes and applications. They define the nanotubes' local physicochemical environment,[8] enable most structural sorting methods,[9−11] control interactions between nanotubes and dissolved chemical species,[12] and in some cases can be made to react with SWCNT sidewalls.[13] For example, methods to intensify and shift SWCNT fluorescence through covalent functionalization reactions require the careful choice of surfactant properties and concentration to properly expose SWCNT surfaces to dissolved reactants.[12,14−16] Many uses of SWCNTs for advanced biomedical sensing rely on coatings that selectively modulate nanotube near-IR fluorescence in the presence of analytes.[17−19] Structure-selective coating interactions between SWCNTs and single-stranded DNA (ssDNA) oligos underlie powerful methods to sort SWCNTs through chromatography or aqueous two-phase partitioning processes.[20−22] SWCNTs coated with ssDNA can also allow detection of metabolites and cancer drugs *in vivo* and guide the nanofabrication of high-performance biotemplated field-effect transistors.[23−26] It is therefore important to gain deeper knowledge of SWCNT coating structures and properties. We report here a valuable tool for such investigations: simple optical measurements that monitor the physisorption of conventional dye molecules to

Received: July 9, 2020
Accepted: August 26, 2020
Published: August 26, 2020

https://dx.doi.org/10.1021/acsnano.0c05720
ACS Nano 2020, 14, 12148−12158

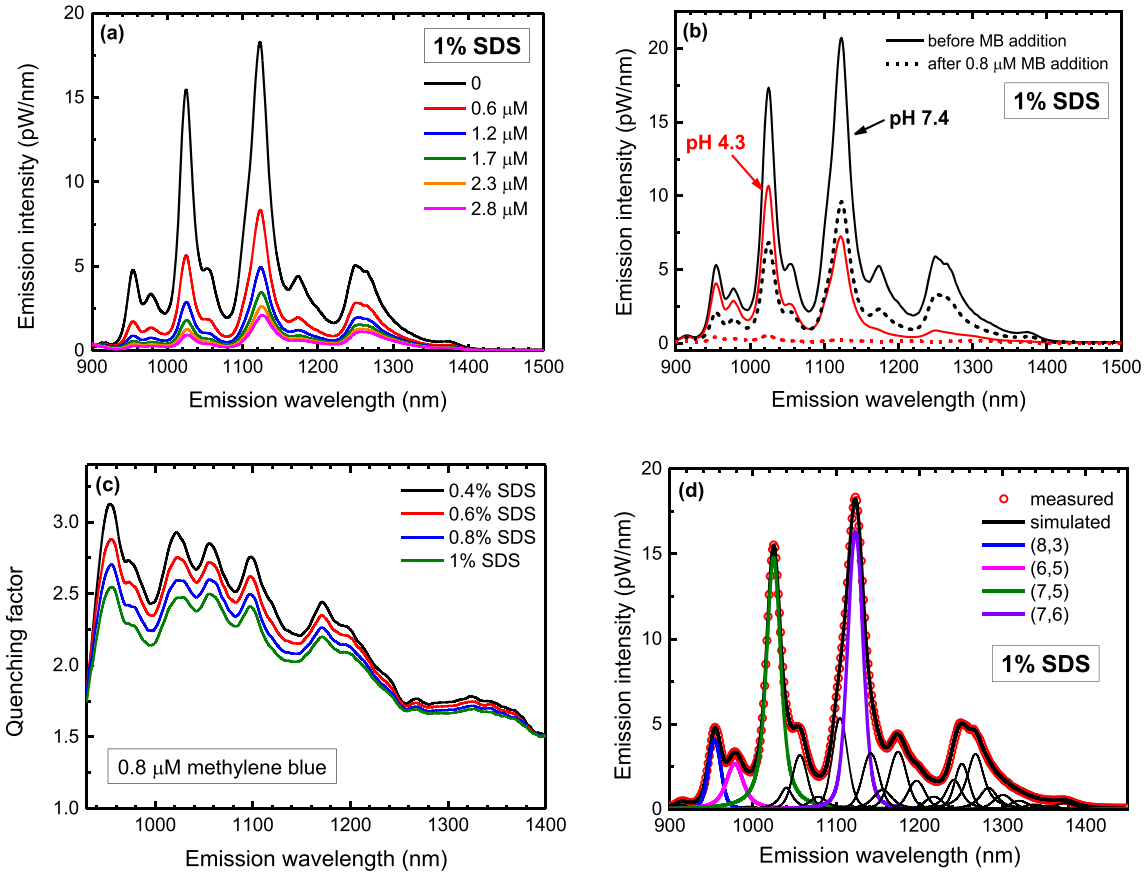

Figure 1. (a) Fluorescence spectra (excited at 642 nm) of a 1% SDS-suspended SWCNT sample with different concentrations of MB, including 0, 0.6, 1.2, 1.7, 2.3, and 2.8 μM. (b) Fluorescence spectra of SWCNT samples dispersed in 1% SDS with pH of 7.4 (solid black curve) and 4.3 (solid red curve). Dashed curves show the corresponding emission spectra in the presence of 0.8 μM MB. (c) Emission spectra with no MB divided by spectra with 0.8 μM MB for SWCNTs suspended in 0.4%, 0.6%, 0.8%, and 1% SDS solutions. (d) Measured (symbols) and simulated (thick black curve) fluorescence spectra of SWCNTs suspended in 1% SDS. Four labeled (n,m) components are shown as thick colored curves; others are shown as thin black curves.

suspended SWCNTs by observing emission quenching of both the dye and nanotubes.

This approach is illustrated with methylene blue (MB), a water-soluble, cationic polynuclear aromatic dye previously shown to form charge-transfer complexes with SWCNTs.[27,28] We find that the visible fluorescence of MB is reversibly quenched by complexation with SWCNTs and that a simple model provides quantitative views of the adsorption equilibrium and the concentration of accessible adsorption sites on SWCNT sidewalls. MB adsorption also quenches the characteristic near-IR fluorescence of semiconducting SWCNTs. Measurements of that quenching in unsorted nanotube samples reveal strong variations among (n,m) species and coatings. These variations are greatest for samples suspended in ssDNA oligos, many of which are known from sorting studies to selectively recognize specific SWCNT species.[21,29,30] The quenching results show how exposure of nanotube surfaces to the surrounding solution depends on coating and on (n,m) species. They also illustrate a simple way to alter the complex fluorescence spectra of SWCNT samples without physical sorting. We complement the experimental study with molecular dynamics simulations of selected ssDNA–SWCNT systems to predict coating structures and estimate contact areas between nanotube and coating. The findings correlate well with the surface exposure patterns deduced from quenching data and provide molecular level insight into the special selectivity of the $(ATT)_4$ ssDNA oligo for (7,5) enantiomers.

RESULTS AND DISCUSSION

Quenching Phenomena. The physisorption of methylene blue (MB) dye molecules on SWCNT surfaces through charge-transfer and hydrophobic interactions leads to the quenching of SWCNT fluorescence and a slight red-shifting of SWCNT absorption (see Figure 1 and Figure S1). Fluorescence intensity of SWCNTs suspended in 1% aqueous sodium dodecyl sulfate (SDS) solution monotonically decreases with increasing addition of MB. In assessing this effect, we corrected for the near-IR tail of MB emission (see Figure S2) by subtracting emission spectra of pure MB solutions. When MB was added to samples of SWCNTs suspended in the strong surfactants sodium dodecylbenzenesulfonate (SDBS) or sodium deoxycholate (SDC), no significant quenching of SWCNT fluorescence was observed. Moreover, the quenched emission from SDS-suspended SWCNTs was restored by addition of SDC to displace SDS from nanotube surfaces (see Figure S3).[6,31] This indicates that the quenching is readily reversible and does not arise from covalent functionalization of MB to SWCNTs. Similar to the recent discovery of fluorescence quenching by dissolved oxygen in ssDNA-coated SWCNTs,[29] we propose that MB-induced quenching is related to the coating quality and

https://dx.doi.org/10.1021/acsnano.0c05720
ACS Nano 2020, 14, 12148–12158

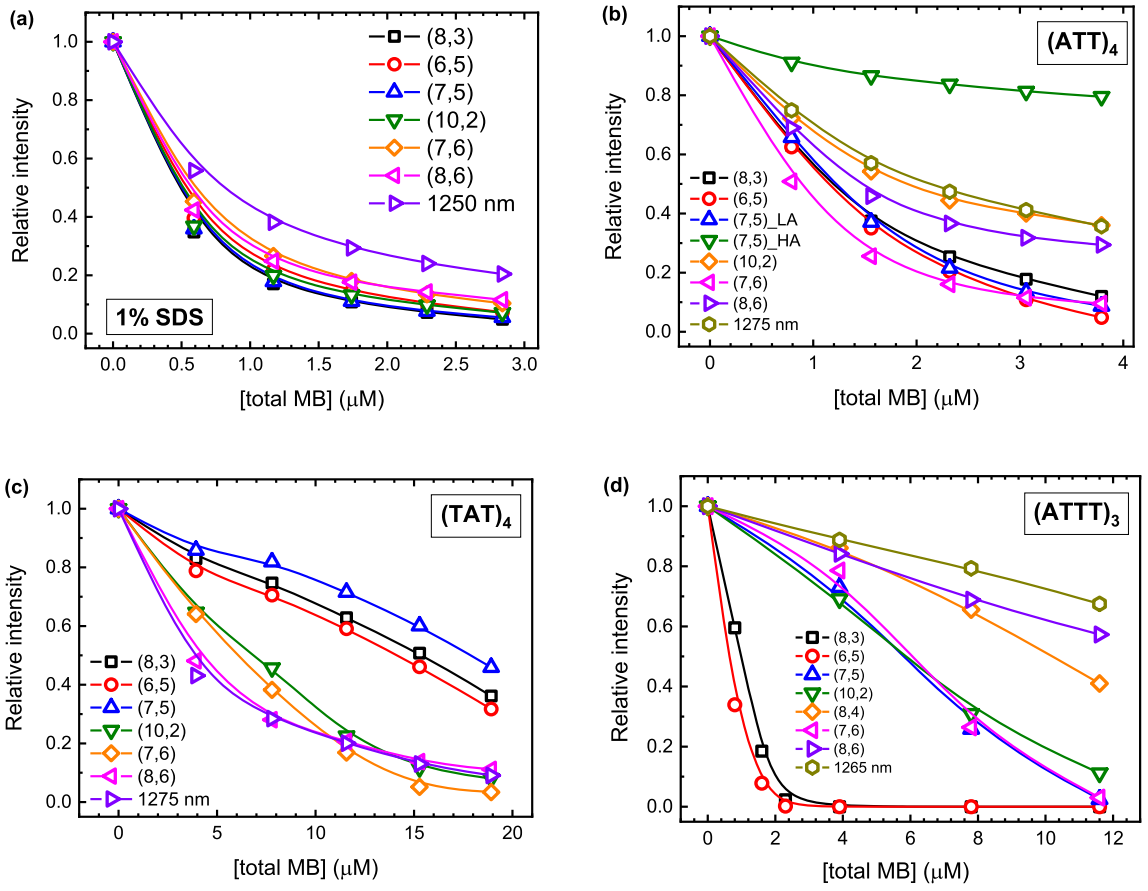

Figure 2. Changes in relative E_{11} emission intensity as a function of total MB concentration for SWCNTs dispersed in solutions of (a) 1% SDS, (b) $(ATT)_4$, (c) $(TAT)_4$, and (d) $(ATTT)_3$. Symbols show measured data points for identified (n,m) species (except for those labeled with emission wavelengths, which contain contributions from several species). Solid curves are guides for the eye.

coverage on nanotube surfaces.[29] Surfactants such as SDBS and SDC provide more complete coverage of SWCNT sidewalls, leaving few sites for physisorption and preventing fluorescence quenching by MB.

It has long been observed that SDS coatings on SWCNTs are very sensitive to pH.[32] Consistent with this, we find that SWCNT fluorescence quenching in SDS dispersions is much greater at pH 4.3 than at pH 7.4 (see Figure 1b). It is also possible to disrupt coating coverage on nanotube surfaces by decreasing surfactant concentration. We accordingly prepared samples with the same SWCNT concentration suspended in 0.4%, 0.6%, 0.8%, and 1% SDS solutions and compared their fluorescence spectra before and after adding 0.8 μM MB. The results are plotted in Figure 1c as quenching spectra, which were obtained by dividing the emission spectrum with MB by that without MB. Note that values in such plots increase from 1 (no quenching) to larger values as quenching increases. The results indicate enhanced quenching at low surfactant concentrations, supporting the interpretation that coating coverage on nanotube surfaces plays a key role in controlling MB adsorption.

The quenching extent also depends on SWCNT concentration (see Figure S4). With the same concentration of added MB, samples with lower SWCNT contents showed enhanced quenching. We interpret this as resulting from an increase in the average number of adsorbed MB molecules per SWCNT at lower nanotube concentrations. When samples with MB and SWCNTs were diluted with surfactant solution only, quenching decreased. This indicates facile desorption of MB and an equilibrium between adsorbed and free species. We observed that other water-soluble dyes such as methylene green and thionine acetate could also quench SWCNT fluorescence.

To investigate the (n,m) dependence of fluorescence quenching by MB, we performed careful deconvolution of the measured fluorescence spectra using an approach developed previously[33−35] to find the underlying emission components and their magnitudes as a function of MB concentration. This deconvolution is illustrated in Figure 1d. We find that emission from each (n,m) species decreases monotonically on adding MB to SDS-suspended SWCNTs (see Figures 1a and 2a). The MB quenching effect is also seen to decrease with increasing SWCNT diameter over the observed range from 0.76 to 1.05 nm (see Figures 1c and 2a).

Structure-Dependent Quenching with ssDNA Coatings. Structure-selective noncovalent interactions between SWCNTs and short ssDNA oligomers have enabled the sorting of SWCNT mixtures into pure (n,m) fractions.[21,22,36] We therefore suspected that MB quenching of ssDNA-suspended SWCNT samples might reveal patterns reflecting (n,m)-specific surface coverages. To test this, we prepared samples of SWCNTs dispersed in solutions of nine different ssDNA oligos: $(GT)_{20}$, $(ATT)_4$, $(TAT)_4$, $(ATTT)_3$, $(GTT)_3G$, $(ATT)_4AT$, $(TTA)_4TT$, $(TGT)_4T$, and $(GT)_6$. The pH values of all samples were stabilized at 7.4 by a Na_2HPO_4/NaH_2PO_4 buffer. For samples in each ssDNA coating, we measured,

https://dx.doi.org/10.1021/acsnano.0c05720
ACS Nano 2020, 14, 12148−12158

Table 1. SWCNT (*n*,*m*) Species That Are Deduced from Quenching Data to Have High or Low Surface Coverage (Relative to Other Species) When Suspended by Various ssDNA Oligos

	$(ATT)_4$	$(TAT)_4$	$(ATTT)_3$	$(ATT)_4AT$	$(TTA)_4TT$	$(GTT)_3G$	$(TGT)_4T$	$(GT)_{20}$	$(GT)_6$
high coverage	$(7,5)_{HA}$	(6,5), (8,3), (7,5)	(8,4), (8,6)	(7,5)	(6,5), (8,3), (7,6)	(7,6)	(10,2)		(10,2)
low coverage			(6,5), (8,3)	(8,3)	(7,5), (10,2), (8,6)			(6,5), (8,3)	

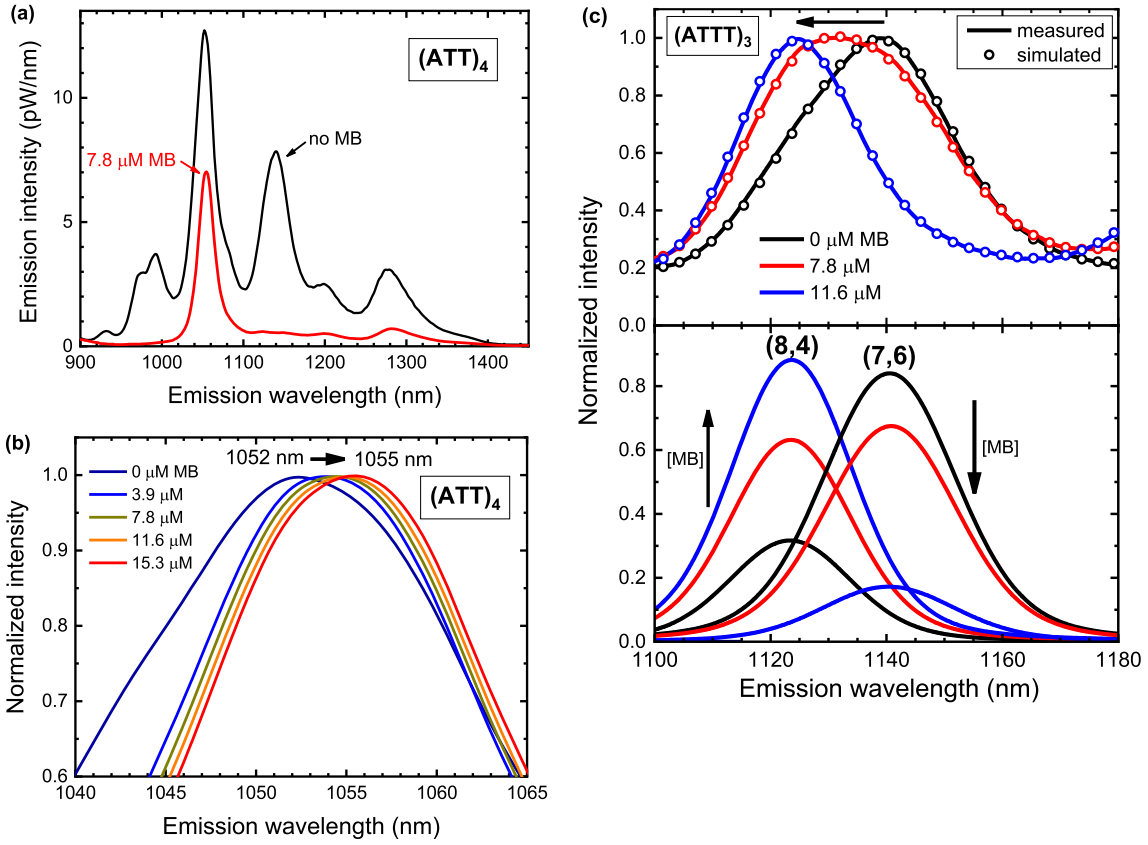

Figure 3. (a) Fluorescence spectra (excited at 642 nm) of unsorted SWCNTs suspended in a $(ATT)_4$ solution in the absence (black curve) and presence (red curve) of 7.8 μM MB. (b) Normalized emission spectra of the sample with MB concentrations ranging from 0 (black curve) to 15.3 μM (red curve). (c) The top frame shows the measured (solid curves) and simulated (symbols) normalized fluorescence spectra of an $(ATTT)_3$-suspended SWCNT sample in the range 1100−1180 nm. The curves were measured with 642 nm excitation and MB concentrations of 0, 7.8, and 11.6 μM. The bottom frame shows the deduced emission components assigned to (8,4) and (7,6) species.

deconvoluted, and compared the SWCNT emission spectra as a function of MB concentration to identify (*n*,*m*) species with unusually strong or weak dye quenching.

$(GT)_{20}$ is an ssDNA oligo commonly selected for SWCNT dispersion. As shown in Figure S5, we found that $(GT)_{20}$-coated nanotubes were significantly quenched by MB, with the small-diameter species (6,5) and (8,3) showing stronger quenching than the others monitored in our sample. We infer that the structure of $(GT)_{20}$ on (6,5) and (8,3) leaves relatively large areas of the nanotube surface exposed for dye adsorption. A more extreme case of (*n*,*m*)-specific low surface coverage was found for $(ATTT)_3$-suspended samples. The results plotted in Figure 2d show that MB quenches emission from (6,5) and (8,3) SWCNTs in $(ATTT)_3$ far more readily than the other species, indicating unusually efficient dye adsorption on those small-diameter SWCNTs.

By contrast, we also observed many instances in which interactions between ssDNA and SWCNTs lead instead to relatively strong protection from dye quenching. In $(ATTT)_3$, MB quenching is notably weak for (8,6) and (8,4) SWCNTs, suggesting high surface coverage (Figure 2d). This selectivity seems consistent with the report by Tu *et al.* of specific recognition of (8,4) by $(ATTT)_3$ in chromatographic sorting studies.[21] We also found selective protection from dye quenching for (6,5), (8,3), and (7,5) dispersed in $(TAT)_4$ (Figure 2c). Hypothesizing that this discrimination might also lead to different buoyant densities of those three nanotubes compared to other (*n*,*m*) species, we performed nonlinear density-gradient ultracentrifugation[37] on a $(TAT)_4$-dispersed unsorted sample (without MB) and successfully extracted those three (*n*,*m*) species from a distinct purple layer that formed in the upper part of the centrifuge tube (see Figure S6). Other cases of selective protection from MB adsorption, interpreted as high surface coverage, were found for (7,6) in $(GTT)_3G$; for (7,5) in $(ATT)_4AT$; for (8,3), (6,5), and (7,6) in $(TTA)_4TT$; and for (10,2) in both $(TGT)_4T$ and $(GT)_6$ (see Figure S5). Similar recognition matches were reported from sorting studies by Tu *et al.*[21] Table 1 summarizes the (*n*,*m*) species we deduced to have relatively high or low surface coverages in the different ssDNA oligos that were studied.

MB quenching of emission from (7,5) SWCNTs in $(ATT)_4$ is of special interest because it was recently reported that the

https://dx.doi.org/10.1021/acsnano.0c05720
ACS Nano 2020, 14, 12148−12158

$(ATT)_4$ coating displacement kinetics differ dramatically between the two optical isomers of (7,5).[31] As shown in Figure 2b, we find that this enantiomeric recognition also makes MB quenching of SWCNT emission much milder for $(7,5)_{HA}$ (the "high-affinity" isomer) than for $(7,5)_{LA}$ ("low-affinity" isomer) or for other (*n*,*m*) species. We conclude that interactions between $(ATT)_4$ and $(7,5)_{HA}$ lead to high surface coverage as well as high binding affinity.

This structure-specific coating interaction can also lead to vivid spectral tailoring of fluorescence from SWCNT samples. When 7.8 μM MB is added to unsorted SWCNTs in $(ATT)_4$, $(7,5)_{HA}$ is uniquely well protected from dye adsorption and emission quenching. With fluorescence from other species suppressed, the resulting spectrum has just one dominant peak, from $(7,5)_{HA}$, that is at least 10 times more intense than other features. This dramatic spectral simplification in an unsorted sample is shown in Figure 3a and Figure S7. A different spectral tailoring can occur in $(ATTT)_3$ because the (6,5) and (8,3) SWCNTs are more readily quenched than other (*n*,*m*) species, as shown in Figure 2d. As a result, short-wavelength fluorescence from an unsorted $(ATTT)_3$ suspension can be quite selectively suppressed by *ca.* 2 μM MB (see Figure S7c). A more subtle spectral effect is the shift in peak (7,5) emission wavelength that accompanies preferential MB quenching of $(7,5)_{LA}$ compared to $(7,5)_{HA}$ in $(ATT)_4$ suspensions. Because the enantiomers have different peak wavelengths in that coating (1044 nm for $(7,5)_{LA}$ and 1055 nm for $(7,5)_{HA}$, see Figure S8), the preferential quenching shifts the composite peak position several nanometers to longer wavelengths. This minor "tuning" effect is illustrated in Figure 3b.

Related MB-induced spectral tuning was also observed for unsorted SWCNT samples suspended in $(ATTT)_3$. The (8,4) and (7,6) species have overlapped emission features with maxima at 1124 and 1140 nm, respectively. Excitation of the mixed sample at 642 nm, which is near resonant with the (7,6) E_{22} transition, gives mainly (7,6) emission and a spectral peak at 1140 nm. But when 7.8 μM MB is present, the $(ATTT)_3$ coating allows preferential dye adsorption on (7,6) compared to (8,4), suppressing the (7,6) fluorescence and causing the emission spectrum to broaden and blue-shift to 1132 nm. With an additional 3.8 μM MB, the (8,4) emission becomes dominant, giving a composite peak at 1124 nm and a total shift of 16 nm. These spectral changes are shown in the top frame of Figure 3c, where the measured data are accurately simulated as superpositions of the two spectra in the lower frame (see also Figure S8).

Modeling of Adsorption and Quenching Extents. To further study the quenching of SWCNT fluorescence by MB, we measured the visible fluorescence from MB molecules in SWCNT solutions. MB molecules physisorb onto SWCNT sidewalls, causing fluorescence quenching of both MB and SWCNTs through a presumed charge-transfer process. We prepared a suspension of SWCNTs in 0.5% carboxymethyl cellulose (CMC),[38] which is thought to allow enhanced adsorption of other species onto nanotube sidewalls. When MB was then added at a concentration of 3.8 μM, we found no detectable emission from MB. This implies that fluorescence of adsorbed MB was nearly completely quenched, so the observed visible emission from other SWCNT samples containing MB may be assigned solely to free MB molecules (see Figure S9). We also prepared samples of $(GT)_{20}$-suspended SWCNTs containing 0, 1.6, and 3.9 μM MB, measured their emission spectra, and then diluted them by a factor of 2. After dilution, the emission decreased to *ca.* 0.53, 0.63, and 0.83 of the original intensities, respectively (see Figure S10). In the pure SWCNT solution, the decrease in fluorescence was slightly smaller than the volumetric dilution factor because SWCNTs reabsorbed some emission through the inner filter effect. However, fluorescence of SWCNTs in samples with MB remained significantly higher than would be expected from the dilution factor, with the highest concentrations of MB showing the least change on dilution. This is further evidence for a dynamic equilibrium between adsorbed and free MB molecules, in which dilution drives the system from adsorbed toward free.

A schematic representation of this dynamic physisorption equilibrium is

$$\text{MB} + \text{SWCNT} \rightleftarrows \text{MB-SWCNT}$$

In this simple model, MB represents free methylene blue molecules, MB-SWCNT represents nanotube sidewall sites with adsorbed methylene blue, and SWCNT represents sidewall sites on the suspended nanotubes available for MB adsorption. Let N_T be the total MB concentration, N_A the adsorbed MB concentration, N_F the free MB concentration, and N_{max} the maximum concentration that can be adsorbed (at saturation). Then, $N_T = N_A + N_F$, and the concentration of unoccupied SWCNT adsorption sites is $(N_{max} - N_A)$. We introduce K as an effective equilibrium constant for MB adsorption:

$$K = \frac{N_A}{N_F(N_{max} - N_A)} \tag{1}$$

At equilibrium, the concentration of free dye molecules is then given by

$$N_F = \frac{N_A}{(N_{max} - N_A)K} \tag{2}$$

.

The concentration of adsorbed MB is given by rearranging eq 1:

$$N_A = \frac{KN_{max}N_F}{1 + KN_F} \tag{3}$$

Finally, substituting $N_A = N_T - N_F$ into eq 2 and solving the resulting quadratic equation, we obtain the following expression for free MB concentration in terms of total and maximum adsorbed MB concentrations:

$$N_F = \frac{1}{2}\left\{\left[N_T - N_{max} - \frac{1}{K}\right] + \sqrt{\left[N_T - N_{max} - \frac{1}{K}\right]^2 + \frac{4N_T}{K}}\right\} \tag{4}$$

Based on our observations with CMC-dispersed nanotubes, we know that MB fluorescence in the presence of SWCNTs reflects only the free MB concentration. The emission from free MB, denoted I_{freeMB}, can therefore be written (based on eq 4) as

$$I_{freeMB} = \frac{S}{2}\left\{\left[N_T - N_{max} - \frac{1}{K}\right] + \sqrt{\left[N_T - N_{max} - \frac{1}{K}\right]^2 + \frac{4N_T}{K}}\right\} \tag{5}$$

where S is a proportionality factor.

In this equilibrium model, N_{max} should depend (proportionally) on SWCNT concentration, but K should not. We

https://dx.doi.org/10.1021/acsnano.0c05720
ACS Nano 2020, 14, 12148−12158

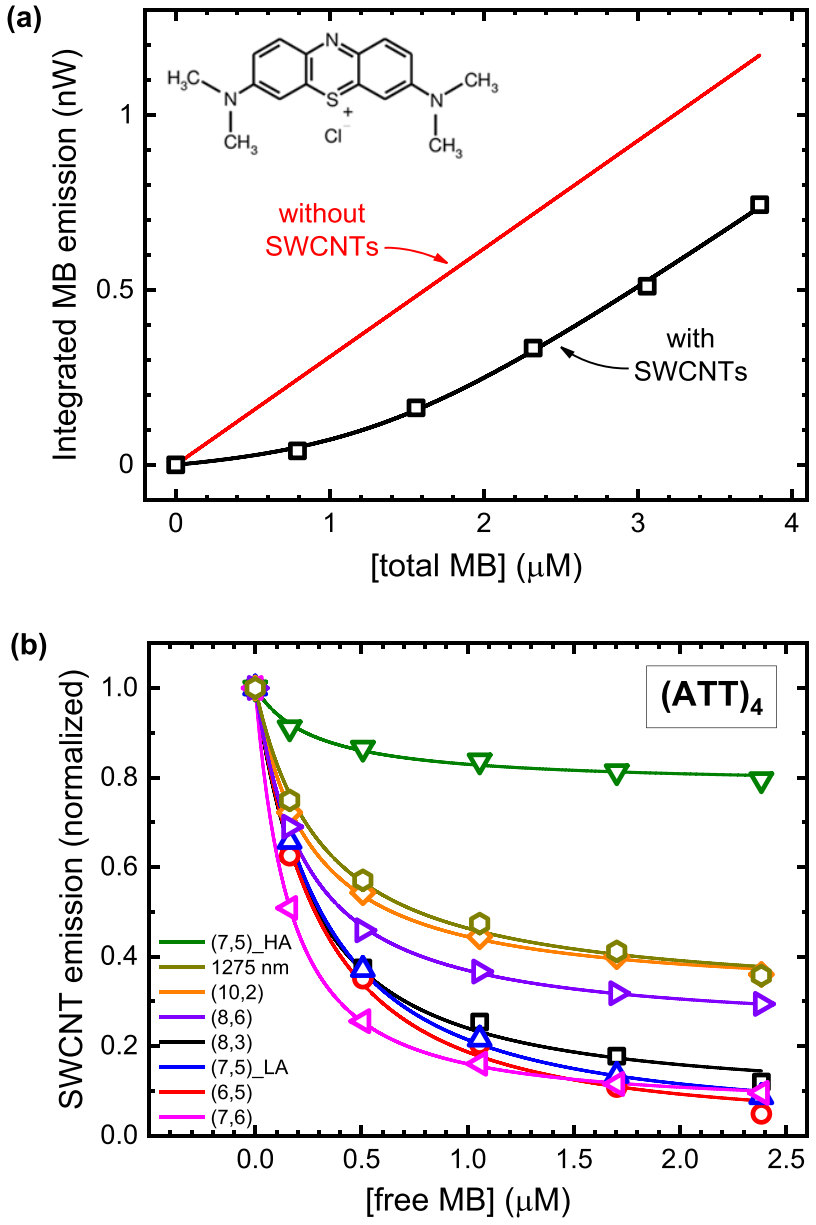

Figure 4. (a) Dependence on total MB concentration of MB fluorescence (integrated from 682 to 700 nm) for MB in an $(ATT)_4$ suspension of SWCNTs (black squares). The red line shows the predicted dependence in the absence of SWCNTs. (b) Normalized E_{11} emission intensity measured for several (n,m) species as a function of free MB concentration in the $(ATT)_4$-suspended SWCNT sample.

applied the model to simulate the dependence of MB fluorescence on total MB concentration in samples of SWCNTs suspended in SDS, CMC, and $(ATT)_4$ solutions (see Figure 4 and Figures S11 and S12). The samples in SDS and CMC had similar integrated SWCNT absorbance from 900 to 1350 nm, indicating similar SWCNT concentrations. However, the deduced N_{max} values were very different: 0.83 μM in SDS and 8.4 μM in CMC (see Figures S11 and S12). We infer that the CMC dispersion leaves SWCNT surfaces much more exposed to dissolved species as compared to SDS and thus gives the larger N_{max} value.

Measurements of MB emission intensity in an $(ATT)_4$ dispersion of SWCNTs are shown as a function of total MB in Figure 4a (black symbols). The solid curve is a fit using eq 5 with parameters N_{max} and K adjusted. In the limit of a high concentration ratio of total MB to SWCNT adsorption sites, $N_F = N_T$, and all MB molecules are free to fluoresce. This gives intensity proportional to total MB concentration:

$$I_{MB} = SN_T \tag{6}$$

as illustrated by the red line in Figure 4a. For other ratios of MB to SWCNT, the concentration of free MB can be deduced from the measured dye fluorescence intensity and value of slope S in eq 6:

$$N_F = \frac{I_{MB}}{S} \tag{7}$$

The other emitter in our system is SWCNTs. To model the quenching of their emission by adsorbed molecules such as MB, we have performed numerical simulations (see details in the Supporting Information). As shown in Figure S13, these predict that, if the adsorbed quenchers are randomly located

https://dx.doi.org/10.1021/acsnano.0c05720
ACS Nano 2020, 14, 12148−12158

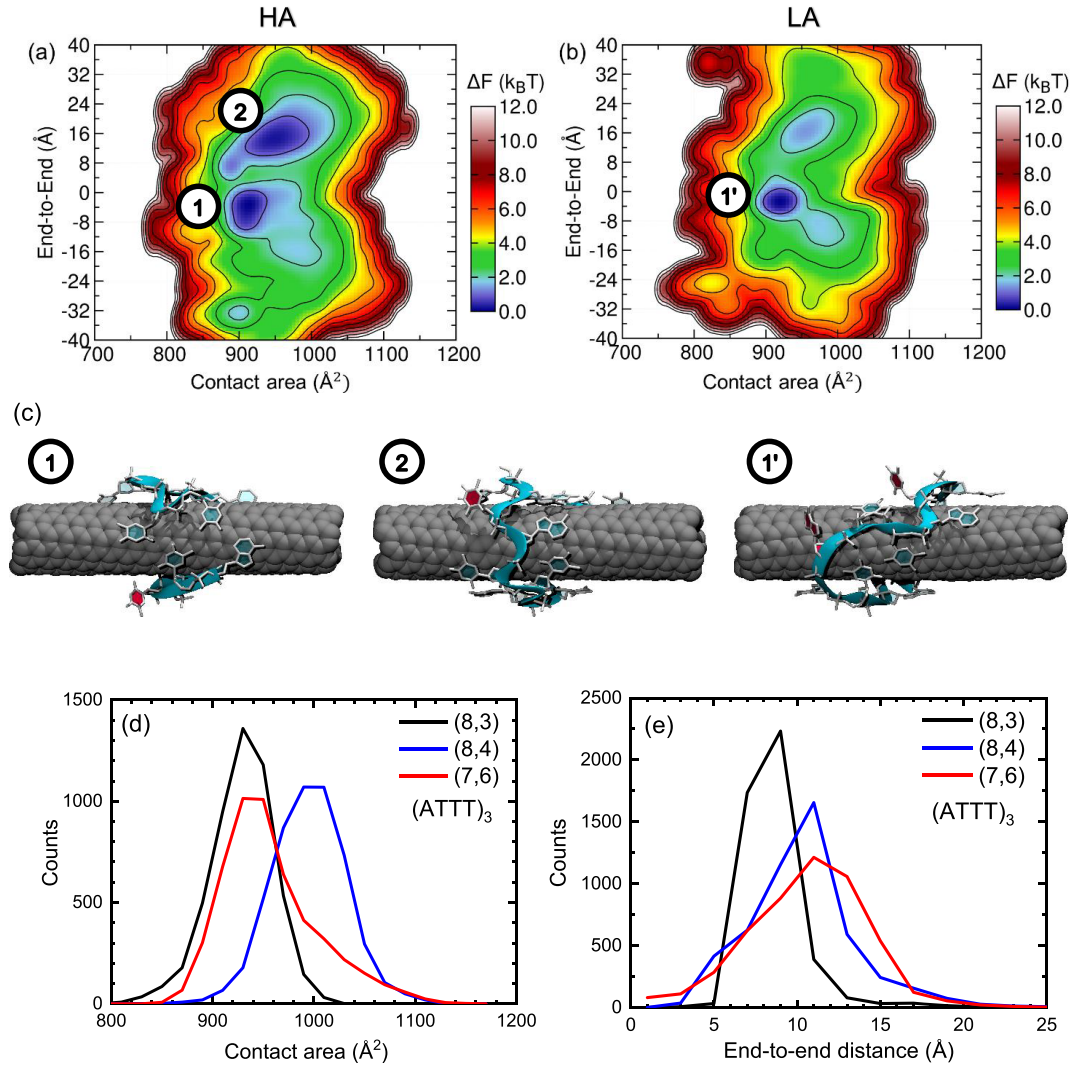

Figure 5. 2D contour plots of free energy vs end-to-end oligo distance and contact area, based on replica exchange molecular dynamics simulations, for $(ATT)_4$ on (a) M, or right-handed (7,5), identified as $(7,5)_{HA}$, and on (b) P, or left-handed (7,5), identified as $(7,5)_{LA}$. Note that origins of the two free energy scales are independent. (c) Representative REMD snapshots of structures at the labeled energy minima in the contour plots above. Nucleobase carbons and SWCNT atoms are drawn in white and gray, respectively. Cyan ribbons show ssDNA backbones. Bases colored red are considered desorbed from the SWCNT surface. Distributions of (d) contact areas and (e) end-to-end distances found from MD simulations of $(ATTT)_3$ on (8,3) (black curves), (8,4) (blue curves), and (7,6) (red curves).

on the sidewalls, SWCNT fluorescence (I_{SWCNT}) varies with number of adsorbed quenchers according to the relation

$$\frac{I_{SWCNT}}{I_0} = \frac{C^2}{(C + N_A)^2} \tag{8}$$

where I_0 is the fluorescence intensity without quenchers, and C is a parameter related to intrinsic SWCNT quenching. Using eq 4 to substitute for N_A, we obtain the following relation that combines SWCNT fluorescence and MB fluorescence (through N_F):

$$\frac{I_{SWCNT}}{I_0} = \frac{1}{\left(1 + \frac{BKN_F}{1 + KN_F}\right)^2} \tag{9}$$

Here, the parameter B equals N_{max}/C.

This quantitative model uses only two parameters (K and B) to describe SWCNT relative emission intensity as a function of free MB concentration. Figure 4b and Figures S11 and S12 show that it can successfully simulate the quenching data measured for six (n,m) species and three coatings. Our results for samples in 1% SDS and CMC reveal significant variations of parameter B with the SWCNT diameter. Because these variations exceed the mild diameter dependence found for exciton range,[39] which would be reflected in parameter C, we will assume B to be approximately proportional to N_{max}. As plotted in Figures S11d and S12d, the deduced density of adsorption sites in SDS and CMC then appears to generally decrease by a factor of ~3 as nanotube diameter increases from ~0.8 to 1.05 nm. In suspensions of $(ATT)_4$, which is known to show quite different affinities for the two enantiomers of (7,5) SWCNTs,[31] the deduced B parameter for $(7,5)_{LA}$ is greater than for $(7,5)_{HA}$ by a factor of 45. Although this large factor may not reliably represent the true ratio of adsorption sites because of limitations in our model, the result does point to a significant difference in surface exposures as the $(ATT)_4$ coating discriminates between (7,5) SWCNT optical isomers. In general, we also note that exposed SWCNT surface regions

https://dx.doi.org/10.1021/acsnano.0c05720
ACS Nano 2020, 14, 12148−12158

that are too small to accommodate MB adsorption will not be probed by our quenching experiments.

Molecular Dynamics Simulations. To gain insight into observed structure-specific ssDNA–SWCNT interactions, we have conducted atomistic simulations using both regular molecular dynamics (MD) and the more extensive replica exchange molecular dynamics (REMD), which have been found useful in prior investigations of ssDNA-wrapped SWCNTs.[40,41] In our first set of simulations, 200 ns MD runs were performed for both (7,5) enantiomers wrapped with the same left-handed $(ATT)_4$ oligo. $(ATT)_4$ maintained its helical structure in both cases, but the dynamics of DNA bases differed on the two isomers. We analyzed trajectories to find the distribution of contact areas between $(ATT)_4$ and nanotube surface, and also the distance between ends of the oligo, as projected along the nanotube axis. Results of our analyses, shown in Figure S15c,d, reveal that end-to-end distances are similar for both enantiomers, but contact areas on the right-handed nanotube enantiomer are significantly larger than on the left-handed one. According to stereochemical convention, these right- and left-handed isomers are designated M and P, respectively.[42] We suggest that the greater contact area on M results in fewer adsorption sites for MB molecules on the nanotube surface and accounts for less efficient quenching by the dye. We therefore assign $(7,5)_{HA}$ as enantiomer M and $(7,5)_{LA}$ as P. Our simulations show that the $(ATT)_4$ oligo has only one desorbed thymine base when wrapped on the $(7,5)_{HA}$ surface but two desorbed thymines on $(7,5)_{LA}$. To quantify this phenomenon, we calculated distances from the nanotube axis to the center-of-mass of every nucleotide (see Figure S15a,b). We also repeated those simulations with completely different starting structures, including a right-handed $(ATT)_4$ conformation, to verify the (7,5) enantiomeric differences in $(ATT)_4$ wrapping (see Figures S16 and S17). Finally, as a control we ran equivalent MD simulations for $(GT)_{20}$ oligos on both (7,5) enantiomers. These results, plotted in Figures S18 and S19, showed no significant enantiomeric differences in contact area, consistent with our experimental results for quenching by MB.

We extended the simulation studies of $(ATT)_4$ on (7,5) using the enhanced sampling method of replica exchange molecular dynamics (REMD). A total of 46 MD simulation replicas at temperatures ranging from 290 to 727 K explored the conformational landscape of $(ATT)_4$ on right-handed and left-handed (7,5) SWCNTs, under well-matched conditions. We then calculated contact areas and end-to-end distances for every frame of the room temperature replica and converted the probabilities to free energy contour plots as a function of those two variables, as shown in Figure 5a,b. The obvious difference between the two contour plots is that the left-handed (7,5) gives a single deep well, but its enantiomer gives two wells of similar depth (and similar populations). Representative molecular structures at the labeled energy minima of the contour plots are illustrated in Figure 5c (see Figure S20 for rear views of these structures). Free energy minimum 2 has a positive end-to-end distance, signifying a left helical DNA structure, whereas minima 1 and 1′ have very small end-to-end distances and a tilted ringlike DNA wrapping. Based on distances of base centers from the SWCNT axis, we estimate that structure 1 has one desorbed base, structure 2 one partially desorbed base, and structure 1′ two desorbed bases. This likely implies stronger binding for the left-handed (7,5) isomer, making it the high-affinity species, $(7,5)_{HA}$. In addition, $(ATT)_4$ on $(7,5)_{HA}$ shows a somewhat greater contact area than on $(7,5)_{LA}$, as is consistent with our findings for quenching by MB. These differences in contact area and base binding agree qualitatively with our results from regular MD simulations and are interpreted as the source of $(ATT)_4$ enantiomer discrimination. We note, however, that our simulations involve only one ssDNA molecule per nanotube segment, so possible effects from interactions among oligos on the surface are not represented.

Our experiments reveal that (8,3) and (6,5) SWCNTs coated by $(ATTT)_3$ are quenched much more efficiently than other species by MB (see Figure 2d), and sorting research has found special recognition of (8,4) by $(ATTT)_3$. To explore the structural basis of these differences, we performed regular MD computations to simulate interactions of the $(ATTT)_3$ oligo with (8,3), (8,4), and (7,6), which differ in quenching efficiency and in diameter. The simulations found $(ATTT)_3$ coating structures with significantly different contact areas in the order (8,3) < (7,6) < (8,4) (see Figure 5d and Table 2).

Table 2. MD Simulation Values for Average Contact Areas and End-to-End Distances of ssDNA Oligos on SWCNT Surfaces

ssDNA oligo	(n,m) species	contact area (Å^2)	end-to-end distance (Å)
$(GT)_{20}$	$(7,5)_{HA}$	3150 ± 69	64.4 ± 4.3
	$(7,5)_{LA}$	3136 ± 52	61.6 ± 3.6
$(ATT)_4$	$(7,5)_{HA}$	984 ± 45	10.0 ± 2.1
	$(7,5)_{LA}$	938 ± 41	10.2 ± 2.1
$(ATTT)_3$	(8,4)	995 ± 35	10.3 ± 3.3
	(7,6)	953 ± 46	10.6 ± 3.7
	(8,3)	932 ± 30	8.6 ± 1.7

This order matches our experimental observations of quenching by MB adsorption but is not predictable from end-to-end distance results or from SWCNT diameters. We conclude that contact area computed from MD simulations is a useful parameter to describe surface coverage differences for ssDNA oligos on SWCNTs.

CONCLUSIONS

Experiments and simulations show that insights into coating coverage on semiconducting SWCNTs can be revealed by measuring the quenching of intrinsic nanotube fluorescence in the presence of dyes such as methylene blue. Such dyes tend to physisorb onto exposed regions of SWCNT sidewalls, greatly reducing the emissive quantum yields of both the dye and the nanotube. For SWCNTs suspended in ssDNA with specific base sequences, particular semiconducting (n,m) species are deduced to have unusually high or unusually low surface coverage compared to other (n,m) species. This structure-selectivity in surface coverage is related to the selective recognition that allows structural sorting of SWCNTs in ssDNA. Methylene blue quenching data clearly show that the $(ATT)_4$ ssDNA oligo strongly discriminates between (7,5) enantiomers. Simple equilibrium modeling allows fitting of quenching data to provide parameters for comparative complexation constants and accessible surface areas. Values of these parameters are found to depend on both (n,m) species and coating identity. These findings are complemented by molecular dynamics simulations of interactions between ssDNA oligos and SWCNTs. The results give computed contact areas that correlate well with the experimental data,

https://dx.doi.org/10.1021/acsnano.0c05720
ACS Nano 2020, 14, 12148–12158

supporting the view that quenching by physisorbed species measures sidewall exposure of the suspended nanotubes.

MATERIALS AND METHODS

Sample Preparation. Approximately 3.5 mg of raw HiPco SWCNTs (Rice University reactor, batch 195.1) was added to 15 mL of 1% (w/v) sodium dodecyl sulfate (SDS). The mixture was tip-sonicated at 5 W output power (3 mm tip, Misonix Microson XL) for 15 active minutes (45 min with duty cycle of 20 s on, 40 s off) while immersed in a room temperature water bath. The suspension was then centrifuged for 90 min at 13 000*g* in a Biofuge-13 instrument (Baxter Scientific), and the supernatant was collected. The same procedure was used to prepare SWCNT suspensions in 0.5% sodium carboxymethyl cellulose (CMC, average MW = 90 000). Custom-synthesized ssDNA was purchased from Sigma-Aldrich. Aqueous solutions of ssDNA were prepared at a fixed concentration of 2 mg/mL in 0.1 M sodium chloride (NaCl) and 0.06 M sodium phosphate buffer (pH = 7.4). Raw HiPco SWCNTs were added to the ssDNA solution and tip-sonicated at 5 W output power for 30 active minutes (90 min with duty cycle of 20 s on, 40 s off) while immersed in an ice−water bath. Samples were then centrifuged for 90 min at 13 000*g* to remove aggregates and impurities. Stock solutions of methylene blue (Fisher Scientific) were prepared at a fixed concentration of 0.4 mM. Methylene green and thionine acetate were purchased from Frontier Scientific and MP Biomedicals, LLC, respectively. An aqueous solution of 5% (w/v) sodium deoxycholate (SDC) was prepared for use in coating displacement.

Sample Characterization. Short-wave infrared (SWIR) fluorescence and absorption spectra were measured in 1 cm path length cells using a prototype model NS2 NanoSpectralyzer instrument (Applied NanoFluorescence, LLC). SWIR fluorescence spectra were excited with three diode lasers at fixed excitation wavelengths of 642, 659, and 784 nm. Visible fluorescence spectra from methylene blue were measured using a prototype NS3 NanoSpectralyzer instrument (Applied NanoFluorescence, LLC) with 638 nm excitation.

Computational Methods. Atomistic molecular dynamics (MD) simulations were used to investigate ssDNA−SWCNT hybrids. Single DNA strands of $(ATTT)_3$, $(ATT)_4$, and $(GT)_{20}$ were initially positioned in a left-handed helical conformation around SWCNT segments. To study the specific affinities of ssDNA−SWCNT hybrid structures, the $(ATTT)_3$ oligo was placed around right-handed segments of (8,3), (8,4), and (7,6) SWCNTs with lengths of 4.0, 4.4, and 4.6 nm, respectively. Enantiomeric differences were explored using strands of $(ATT)_4$ and $(GT)_{20}$ placed on left- and right-handed (7,5) SWCNT segments. Those segments were 4.4 nm for $(ATT)_4$ and 8.8 nm for $(GT)_{20}$. In addition, to check that our simulation results did not depend on the initial DNA conformation, we repeated the MD simulation of the $(ATT)_4$−(7,5) hybrid starting with right-handed (instead of left-handed) DNA. SWCNT structures were constructed using VMD,[43] and the initial DNA helix structures, including desorbed bases, were constructed in Materials Studio (Biovia). All of the ssDNA−SWCNT hybrids were solvated in TIP3P model water and 100 mM NaCl (to neutralize the prepared systems) with Solvate and Ionize VMD plugins. The systems with 12-mer DNA oligos were finally composed of at least 7000 atoms in 3.8 × 3.8 × 5.6 nm boxes. For the $(GT)_{20}$ oligo, the system was composed of 11 500 atoms in a 3.8 × 3.8 × 9.6 nm box.

We used the NAMD 2.12 package[44] to perform MD simulations in which the CHARMM36 force field was applied to describe inter- and intramolecular interactions.[45,46] Temperature and pressure in the simulations were kept constant at 300 K and 1 bar (close to the experimental conditions) through Langevin dynamics with Langevin constant $\gamma_{Lang} = 1.0\ ps^{-1}$ in the NPT ensemble. Long-range Coulomb interaction energies were evaluated using the particle mesh Ewald (PME) method in simulations for which periodic boundary conditions were applied in all directions.[47] The integration time step for simulations was 2.0 fs. Before production runs, 1000 steps of energy minimization and 2 ns of equilibration simulations were conducted, during which ssDNA−SWCNT was restrained by applying a 1 kcal/(mol Å^2) harmonic force constant. Then, 100 ns production runs were performed, and the first 10 ns of trajectories were discarded before performing data analysis.

In every frame, we calculated the distance projected along the nanotube axis between centers of mass of the two end DNA residues and then constructed histograms of those distances. Similar histograms were also prepared showing radial distances between the center-of-mass of every ssDNA nucleotide and the SWCNT axis. To classify bases as adsorbed or desorbed, we selected a threshold separation of 0.85 nm based on the bimodal distributions shown in Figure S15. Varying this threshold by 10% did not qualitatively change our findings. We evaluated the contact area between ssDNA and SWCNT using the VMD plugin for solvent accessible surface area (SASA) and the following equation:

$$\frac{a_{ssDNA}(t) + a_{SWCNT}(t) - a_{ssDNA-SWCNT}(t)}{2} \tag{10}$$

where $a_{ssDNA}(t)$, $a_{SWCNT}(t)$, and $a_{ssDNA-SWCNT}(t)$ represent the SASA values of ssDNA, SWCNT, and ssDNA−SWCNT hybrid at a simulation time t. The van der Waals radius of atoms was taken as 0.14 nm in all contact area calculations. Average end-to-end distances and contact areas were calculated over the final 90 ns of MD trajectories.

Replica exchange MD (REMD) was performed to compare the energy landscapes of $(ATT)_4$ on the two (7,5) enantiomers. Previous reports suggest that REMD is a robust method to investigate DNA−SWCNT interactions.[48−50] Each system was solvated in a 3.61 × 3.61 × 4.40 nm^3 box with a sodium chloride concentration of 0.1 M for consistency with experimental conditions. In addition to sodium counterions, there were 1728 water molecules and 20 Na^+ and Cl^- ions in the box. Both simulations applied periodic boundary conditions in three dimensions, so that the SWCNT ends were in contact with their periodic images. The systems were subjected to energy minimization and 100 ps NVT simulations to heat the systems to room temperature (the initial temperature). REMD simulations were also performed in an NVT ensemble in which an average exchange ratio of 25% was maintained by choosing 54 replicas, the temperature range 290−727 K, and an exchange time of 2 ps. A time step of 2 fs was used, and trajectories were saved every 2 ps. For each replica, we ran a 160 ns simulation and obtained 80 000 configurations. The total simulation time for every REMD simulation was thus 54 × 160 ns = 8.64 μs. To allow a comparison with room temperature experimental results, the room temperature replicas were analyzed (after discarding the first 10 000 configurations) to construct the free energy landscapes shown in Figure 5. The axes are two independent reaction coordinates: end-to-end distance and contact area. Free energies were found from the formulas

$$\Delta G(x, y) = -k_B T \ln(Z) \quad Z = \frac{P(x, y)}{P_{max}(x, y)} \tag{11}$$

where $P(x, y)$ is the joint probability distribution for reaction coordinates x and y, and $P_{max}(x, y)$ is the maximum value of that joint probability.

ASSOCIATED CONTENT

Supporting Information

The Supporting Information is available free of charge at https://pubs.acs.org/doi/10.1021/acsnano.0c05720.

Additional spectra showing quenching by MB; quenching data for suspensions in several ssDNA oligos; description of nonlinear DGU sorting method, SWCNT emission spectra altered by MB; deconvolution of fluorescence spectra; dilution spectra; quantitative analysis of MB quenching of samples in SDS and CMC; numerical simulation of quenching by randomly positioned quenchers in one dimension; evidence of energy transfer from MB to SWCNTs; and trajectory

https://dx.doi.org/10.1021/acsnano.0c05720
ACS Nano 2020, 14, 12148−12158

analyses and structural snapshots from MD and REMD simulations (PDF)

AUTHOR INFORMATION

Corresponding Author

R. Bruce Weisman − *Department of Chemistry and the Smalley-Curl Institute and Department of Materials Science and NanoEngineering, Rice University, Houston, Texas 77005, United States;* orcid.org/0000-0001-8546-9980; Phone: 713-348-3709; Email: weisman@rice.edu; Fax: 713-348-5155

Authors

Yu Zheng − *Department of Chemistry and the Smalley-Curl Institute, Rice University, Houston, Texas 77005, United States;* orcid.org/0000-0003-2703-9143

Ali A. Alizadehmojarad − *Department of Chemistry and the Smalley-Curl Institute, Rice University, Houston, Texas 77005, United States;* orcid.org/0000-0001-6806-5415

Sergei M. Bachilo − *Department of Chemistry and the Smalley-Curl Institute, Rice University, Houston, Texas 77005, United States;* orcid.org/0000-0001-5236-1383

Anatoly B. Kolomeisky − *Department of Chemistry and the Smalley-Curl Institute, Rice University, Houston, Texas 77005, United States;* orcid.org/0000-0001-5677-6690

Complete contact information is available at: https://pubs.acs.org/10.1021/acsnano.0c05720

Notes

The authors declare the following competing financial interest(s): R.B.W. has a financial interest in Applied NanoFluorescence, LLC, which manufactures some of the instruments in this project.

ACKNOWLEDGMENTS

This research was supported by grants from the National Science Foundation (CHE-1803066) and the Welch Foundation (C-0807 and C-1559). We are grateful to the Texas Advanced Computing Center (TACC) for providing computer time for this project.

REFERENCES

(1) Saito, R.; Dresselhaus, G.; Dresselhaus, M. S. *Physical Properties of Carbon Nanotubes*; Imperial College Press: London, 1998.

(2) O'Connell, M. J.; Bachilo, S. M.; Huffman, C. B.; Moore, V.; Strano, M. S.; Haroz, E.; Rialon, K.; Boul, P. J.; Noon, W. H.; Kittrell, C.; Ma, J.; Hauge, R. H.; Weisman, R. B.; Smalley, R. E. Band-Gap Fluorescence from Individual Single-Walled Carbon Nanotubes. *Science* **2002**, *297*, 593−596.

(3) Moore, V. C.; Strano, M. S.; Haroz, E. H.; Hauge, R. H.; Smalley, R. E.; Schmidt, J.; Talmon, Y. Individually Suspended Single-Walled Carbon Nanotubes in Various Surfactants. *Nano Lett.* **2003**, *3*, 1379−1382.

(4) Richard, C.; Balavoine, F.; Schultz, P.; Ebbesen, T. W.; Mioskowski, C. Supramolecular Self-Assembly of Lipid Derivatives on Carbon Nanotubes. *Science* **2003**, *300*, 775−778.

(5) Zheng, M.; Jagota, A.; Semke, E. D.; Diner, B. A.; McLean, R. S.; Lustig, S. R.; Richardson, R. E.; Tassi, N. G. DNA-Assisted Dispersion and Separation of Carbon Nanotubes. *Nat. Mater.* **2003**, *2*, 338−342.

(6) Wenseleers, W.; Vlasov, I. I.; Goovaerts, E.; Obraztsova, E. D.; Lobach, A. S.; Bouwen, A. Efficient Isolation and Solubilization of Pristine Single-Walled Nanotubes in Bile Salt Micelles. *Adv. Funct. Mater.* **2004**, *14*, 1105−1112.

(7) Zheng, Y.; Sanchez, S. R.; Bachilo, S. M.; Weisman, R. B. Indexing the Quality of Single-Wall Carbon Nanotube Dispersions Using Absorption Spectra. *J. Phys. Chem. C* **2018**, *122*, 4681−4690.

(8) Gao, Z.; Danné, N.; Godin, A. G.; Lounis, B.; Cognet, L. Evaluation of Different Single-Walled Carbon Nanotube Surface Coatings for Single-Particle Tracking Applications in Biological Environments. *Nanomaterials* **2017**, *7*, 393.

(9) Hersam, M. C. Progress towards Monodisperse Single-Walled Carbon Nanotubes. *Nat. Nanotechnol.* **2008**, *3*, 387−394.

(10) Zeng, X.; Yang, D.; Liu, H.; Zhou, N.; Wang, Y.; Zhou, W.; Xie, S.; Kataura, H. Detecting and Tuning the Interactions between Surfactants and Carbon Nanotubes for Their High-Efficiency Structure Separation. *Adv. Mater. Interfaces* **2018**, *5*, 1700727.

(11) Fagan, J. A. Aqueous Two-Polymer Phase Extraction of Single-Wall Carbon Nanotubes Using Surfactants. *Nanoscale Adv.* **2019**, *1*, 3307−3324.

(12) Lin, C.-W.; Bachilo, S. M.; Zheng, Y.; Tsedev, U.; Huang, S.; Weisman, R. B.; Belcher, A. M. Creating Fluorescent Quantum Defects in Carbon Nanotubes Using Hypochlorite and Light. *Nat. Commun.* **2019**, *10*, 2874.

(13) Zheng, Y.; Bachilo, S. M.; Weisman, R. B. Controlled Patterning of Carbon Nanotube Energy Levels by Covalent DNA Functionalization. *ACS Nano* **2019**, *13*, 8222−8228.

(14) Ghosh, S.; Bachilo, S. M.; Simonette, R. A.; Beckingham, K. M.; Weisman, R. B. Oxygen Doping Modifies Near-Infrared Band Gaps in Fluorescent Single-Walled Carbon Nanotubes. *Science* **2010**, *330*, 1656−1659.

(15) Piao, Y.; Meany, B.; Powell, L. R.; Valley, N.; Kwon, H.; Schatz, G. C.; Wang, Y. Brightening of Carbon Nanotube Photoluminescence through the Incorporation of sp^3 Defects. *Nat. Chem.* **2013**, *5*, 840−845.

(16) Brozena, A. H.; Kim, M.; Powell, L. R.; Wang, Y. H. Controlling the Optical Properties of Carbon Nanotubes with Organic Colour-Centre Quantum Defects. *Nature Reviews Chemistry* **2019**, *3*, 375−392.

(17) Xu, Y.; Pehrsson, P. E.; Chen, L.; Zhang, R.; Zhao, W. Double-Stranded DNA Single-Walled Carbon Nanotube Hybrids for Optical Hydrogen Peroxide and Glucose Sensing. *J. Phys. Chem. C* **2007**, *111*, 8638−8643.

(18) Barone, P. W.; Baik, S.; Heller, D. A.; Strano, M. S. Near-Infrared Optical Sensors Based on Single-Walled Carbon Nanotubes. *Nat. Mater.* **2004**, *4*, 86−92.

(19) Bisker, G.; Bakh, N. A.; Lee, M. A.; Ahn, J.; Park, M.; O'Connell, E. B.; Iverson, N. M.; Strano, M. S. Insulin Detection Using a Corona Phase Molecular Recognition Site on Single-Walled Carbon Nanotubes. *ACS Sensors* **2018**, *3*, 367−377.

(20) Zheng, M.; Jagota, A.; Strano, M. S.; Santos, A. P.; Barone, P.; Chou, S. G.; Diner, B. A.; Dresselhaus, M. S.; Mclean, R. S.; Onoa, G. B.; Samsonidze, G. G.; Semke, E. D.; Usrey, M.; Walls, D. J. Structure-Based Carbon Nanotube Sorting by Sequence-Dependent DNA Assembly. *Science* **2003**, *302*, 1545−1548.

(21) Tu, X.; Manohar, S.; Jagota, A.; Zheng, M. DNA Sequence Motifs for Structure-Specific Recognition and Separation of Carbon Nanotubes. *Nature* **2009**, *460*, 250−253.

(22) Ao, G.; Khripin, C. Y.; Zheng, M. DNA-Controlled Partition of Carbon Nanotubes in Polymer Aqueous Two-Phase Systems. *J. Am. Chem. Soc.* **2014**, *136*, 10383−10392.

(23) Harvey, J. D.; Jena, P. V.; Baker, H. A.; Zerze, G. H.; Williams, R. M.; Galassi, T. V.; Roxbury, D.; Mittal, J.; Heller, D. A. A Carbon Nanotube Reporter of Microrna Hybridization Events *In Vivo*. *Nat. Biomed. Eng.* **2017**, *1*, 0041.

(24) Harvey, J. D.; Williams, R. M.; Tully, K. M.; Baker, H. A.; Shamay, Y.; Heller, D. A. An *In Vivo* Nanosensor Measures Compartmental Doxorubicin Exposure. *Nano Lett.* **2019**, *19*, 4343−4354.

(25) Sun, W.; Shen, J.; Zhao, Z.; Arellano, N.; Rettner, C.; Tang, J.; Cao, T.; Zhou, Z.; Ta, T.; Streit, J. K.; Fagan, J. A.; Schaus, T.; Zheng, M.; Han, S.-J.; Shih, W. M.; Maune, H. T.; Yin, P. Precise Pitch-

Scaling of Carbon Nanotube Arrays within Three-Dimensional DNA Nanotrenches. *Science* **2020**, *368*, 874−877.
(26) Zhao, M.; Chen, Y.; Wang, K.; Zhang, Z.; Streit, J. K.; Fagan, J. A.; Tang, J.; Zheng, M.; Yang, C.; Zhu, Z.; Sun, W. DNA-Directed Nanofabrication of High-Performance Carbon Nanotube Field-Effect Transistors. *Science* **2020**, *368*, 878−881.
(27) Yan, Y.; Zhang, M.; Gong, K.; Su, L.; Guo, Z.; Mao, L. Adsorption of Methylene Blue Dye onto Carbon Nanotubes: A Route to an Electrochemically Functional Nanostructure and Its Layer-by-Layer Assembled Nanocomposite. *Chem. Mater.* **2005**, *17*, 3457−3463.
(28) Chagovets, V. V.; Kosevich, M. V.; Stepanian, S. G.; Boryak, O. A.; Shelkovsky, V. S.; Orlov, V. V.; Leontiev, V. S.; Pokrovskiy, V. A.; Adamowicz, L.; Karachevtsev, V. A. Noncovalent Interaction of Methylene Blue with Carbon Nanotubes: Theoretical and Mass Spectrometry Characterization. *J. Phys. Chem. C* **2012**, *116*, 20579−20590.
(29) Zheng, Y.; Bachilo, S. M.; Weisman, R. B. Quenching of Single-Walled Carbon Nanotube Fluorescence by Dissolved Oxygen Reveals Selective Single-Stranded DNA Affinities. *J. Phys. Chem. Lett.* **2017**, *8*, 1952−1955.
(30) Shankar, A.; Mittal, J.; Jagota, A. Binding between DNA and Carbon Nanotubes Strongly Depends Upon Sequence and Chirality. *Langmuir* **2014**, *30*, 3176−3183.
(31) Zheng, Y.; Bachilo, S. M.; Weisman, R. B. Enantiomers of Single-Wall Carbon Nanotubes Show Distinct Coating Displacement Kinetics. *J. Phys. Chem. Lett.* **2018**, *9*, 3793−3797.
(32) Strano, M. S.; Huffman, C. B.; Moore, V. C.; O'Connell, M. J.; Haroz, E. H.; Hubbard, J.; Miller, M.; Rialon, K.; Kittrell, C.; Ramesh, S.; Hauge, R. H.; Smalley, R. E. Reversible, Band-Gap-Selective Protonation of Single-Walled Carbon Nanotubes in Solution. *J. Phys. Chem. B* **2003**, *107*, 6979−6985.
(33) Bachilo, S. M.; Strano, M. S.; Kittrell, C.; Hauge, R. H.; Smalley, R. E.; Weisman, R. B. Structure-Assigned Optical Spectra of Single-Walled Carbon Nanotubes. *Science* **2002**, *298*, 2361−2366.
(34) Weisman, R. B.; Bachilo, S. M. Dependence of Optical Transition Energies on Structure for Single-Walled Carbon Nanotubes in Aqueous Suspension: An Empirical Kataura Plot. *Nano Lett.* **2003**, *3*, 1235−1238.
(35) Rocha, J. D.; Bachilo, S. M.; Ghosh, S.; Arepalli, S.; Weisman, R. B. Efficient Spectrofluorimetric Analysis of Single-Walled Carbon Nanotube Samples. *Anal. Chem.* **2011**, *83*, 7431−7437.
(36) Ao, G.; Streit, J. K.; Fagan, J. A.; Zheng, M. Differentiating Left- and Right-Handed Carbon Nanotubes by DNA. *J. Am. Chem. Soc.* **2016**, *138*, 16677−16685.
(37) Ghosh, S.; Bachilo, S. M.; Weisman, R. B. Advanced Sorting of Single-Walled Carbon Nanotubes by Nonlinear Density-Gradient Ultracentrifugation. *Nat. Nanotechnol.* **2010**, *5*, 443−450.
(38) Riou, I.; Bertoncini, P.; Bizot, H.; Mevellec, J. Y.; Buléon, A.; Chauvet, O. Carboxymethylcellulose/Single Walled Carbon Nanotube Complexes. *J. Nanosci. Nanotechnol.* **2009**, *9*, 6176−6180.
(39) Siitonen, A. J.; Tsyboulski, D. A.; Bachilo, S. M.; Weisman, R. B. Dependence of Exciton Mobility on Structure in Single-Walled Carbon Nanotubes. *J. Phys. Chem. Lett.* **2010**, *1*, 2189−2192.
(40) Roxbury, D.; Mittal, J.; Jagota, A. Molecular-Basis of Single-Walled Carbon Nanotube Recognition by Single-Stranded DNA. *Nano Lett.* **2012**, *12*, 1464−1469.
(41) Roxbury, D.; Jagota, A.; Mittal, J. Structural Characteristics of Oligomeric DNA Strands Adsorbed onto Single-Walled Carbon Nanotubes. *J. Phys. Chem. B* **2013**, *117*, 132−140.
(42) Komatsu, N. Stereochemistry of Carbon Nanotubes. *Jpn. J. Appl. Phys.* **2010**, *49*, 02BC01.
(43) Humphrey, W.; Dalke, A.; Schulten, K. VMD: Visual Molecular Dynamics. *J. Mol. Graphics* **1996**, *14*, 33−38.
(44) Phillips, J. C.; Braun, R.; Wang, W.; Gumbart, J.; Tajkhorshid, E.; Villa, E.; Chipot, C.; Skeel, R. D.; Kalé, L.; Schulten, K. Scalable Molecular Dynamics with NAMD. *J. Comput. Chem.* **2005**, *26*, 1781−1802.
(45) Denning, E. J.; Priyakumar, U. D.; Nilsson, L.; Mackerell, A. D., Jr. Impact of 2'-Hydroxyl Sampling on the Conformational Properties of RNA: Update of the CHARMM All-Atom Additive Force Field for RNA. *J. Comput. Chem.* **2011**, *32*, 1929−1943.
(46) Hart, K.; Foloppe, N.; Baker, C. M.; Denning, E. J.; Nilsson, L.; MacKerell, A. D. Optimization of the CHARMM Additive Force Field for DNA: Improved Treatment of the Bi/Bii Conformational Equilibrium. *J. Chem. Theory Comput.* **2012**, *8*, 348−362.
(47) Darden, T.; York, D.; Pedersen, L. Particle Mesh Ewald: An Nlog(N) Method for Ewald Sums in Large Systems. *J. Chem. Phys.* **1993**, *98*, 10089−10092.
(48) Johnson, R. R.; Kohlmeyer, A.; Johnson, A. T. C.; Klein, M. L. Free Energy Landscape of a DNA - Carbon Nanotube Hybrid Using Replica Exchange Molecular Dynamics. *Nano Lett.* **2009**, *9*, 537−541.
(49) Beyene, A. G.; Alizadehmojarad, A. A.; Dorlhiac, G.; Goh, N.; Streets, A. M.; Král, P.; Vuković, L.; Landry, M. P. Ultralarge Modulation of Fluorescence by Neuromodulators in Carbon Nanotubes Functionalized with Self-Assembled Oligonucleotide Rings. *Nano Lett.* **2018**, *18*, 6995−7003.
(50) Alizadehmojarad, A. A.; Zhou, X.; Beyene, A. G.; Chacon, K. E.; Sung, Y.; Pinals, R. L.; Landry, M. P.; Vuković, L. Binding Affinity and Conformational Preferences Influence Kinetic Stability of Short Oligonucleotides on Carbon Nanotubes. *Adv. Mater. Interfaces* **2020**, *7*, 2000353.

https://dx.doi.org/10.1021/acsnano.0c05720
ACS Nano 2020, 14, 12148−12158